A least squares augmented immersed interface method for solving Navier–Stokes and Darcy coupling equations

Zhilin Li [a,*], Ming-Chih Lai [b], Xiaofei Peng [c], Zhiyue Zhang [d]

[a] Center for Research in Scientific Computation (CRSC) and Department of Mathematics, North Carolina State University, Raleigh, NC 27695, USA
[b] Department of Applied Mathematics, National Chiao Tung University, Taiwan
[c] School of Mathematical Sciences South China Normal University, Guangzhou 510631, China
[d] School of Mathematical Sciences, Nanjing Normal University, Nanjing 210023, China

ARTICLE INFO

ABSTRACT

A new finite difference method based on Cartesian meshes and fast Poisson/Helmholtz solvers is proposed to solve the coupling of a fluid flow modeled by the incompressible Navier–Stokes equations and a porous media modeled by the Darcy's law. The finite difference discretization in time is based on the pressure Poisson equation formulation. At each time step, several augmented variables along the interface between the fluid flow and the porous media are introduced so that the coupled equations can be decoupled into several Poisson/Helmholtz equations with those augmented variables acting as jumps of the unknown solution and some directional derivatives. The augmented variables should be chosen so that the Beavers–Joseph–Saffman (BJS) or Beavers–Joseph (BJ) and other interface conditions are satisfied. It has been tested that a direct extension of the augmented idea in [27] does not work well when the fluid flow is modeled by the Navier–Stokes equations. One of the new ideas of this paper is to enforce the divergence free condition at the interface from the fluid side. In this way, the Schur complement matrix for the augmented variables is over-determined and the least squares solution is used for the coupling problem. The new augmented approach enables us to solve the Navier–Stokes and Darcy coupling efficiently with second order accurate velocity and pressure in the L^∞ norm for tested problems. The proposed new idea in enforcing the divergence free condition at the interface from the fluid side has also been utilized to solve the Stokes and Darcy coupling equations and shown to outperform the original method in [27]. In additional to the detailed accuracy check for the present method, some interesting numerical simulations for Navier–Stokes and Darcy coupling have been conducted in this paper as well.

1. Introduction

In this paper, we intend to find numerical solutions for the coupling of a fluid flow and porous media. For self-contained purpose, we state the governing equations, the boundary and interface conditions, and the physical parameters in detail although they have appeared in the literature.

The fluid flow is modeled by the incompressible Navier–Stokes equations,

$$\rho_f \left(\frac{\partial \mathbf{u}_f}{\partial t} + \mathbf{u}_f \cdot \nabla \mathbf{u}_f \right) + \nabla p_f = \mu_f \Delta \mathbf{u}_f + \mathbf{F}, \qquad \mathbf{x} \in \Omega_f, \qquad (1)$$
$$\nabla \cdot \mathbf{u}_f = 0,$$

where $\mathbf{u}_f$ is the fluid velocity, p_f is the pressure, and $\mathbf{F} = (F_1, F_2)$ is an external body force. The physical parameters $\mu_f > 0$ and $\rho_f > 0$ are the viscosity and density of the fluid, respectively, which are assumed to be constant in Ω_f. The porous media is modeled by the Darcy's law as

$$\mathbf{u}_D = -\frac{K}{\mu_D} \nabla p_D = -K_1 \nabla p_D, \qquad\qquad \mathbf{x} \in \Omega_D, \qquad (2)$$
$$\nabla \cdot \mathbf{u}_D = 0,$$

where $\mathbf{u}_D$ and p_D are the corresponding fluid velocity and the pressure in the porous media, and K is the permeability which is assumed to be a constant in this paper. For simplicity, we set $K_1 = K/\mu_D$. Note that, the numerical method presented in this paper can be extended to add a fluid source term such as $\nabla \cdot \mathbf{u}_D = \phi$ in the porous media region without much difficulties.

Fig. 1 illustrates the coupling problem in which a porous media is modeled by the Darcy's law inside of a closed interface Γ while an incompressible fluid flow is modeled by the Navier–

* Corresponding author.
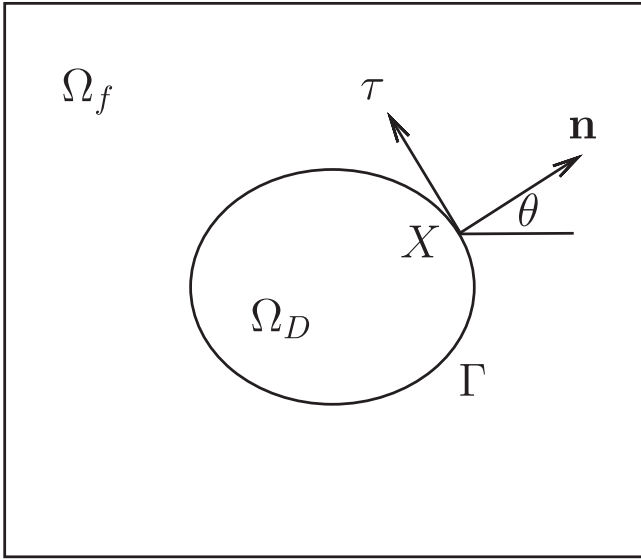*E-mail addresses:* zhilin@math.ncsu.edu, zhilin@ncsu.edu (Z. Li).

Fig. 1. A diagram of a fluid flow and porous media. In the diagram, **n** and $\boldsymbol{\tau}$ are the unit normal and tangential directions, respectively.

Stokes equations outside of the interface. We assume that the velocity is prescribed along the outer boundary $\partial \Omega_f$ (either no-slip or given flow boundary conditions). Our method can also handle the case where the fluid flow is inside while the Darcy's law is outside. In such a case, the velocity normal component $\mathbf{u}_D \cdot \mathbf{n}$ is usually prescribed along the outer boundary $\partial \Omega_D$. Notice that, it is equivalent to impose the normal derivative of the pressure as $\frac{\partial p_D}{\partial n} = -\mathbf{u}_D \cdot \mathbf{n}/K_1$. The well-posedness and regularity of the above coupling problem has been investigated in the literature such as in [25] and the references therein.

The relation of velocity and pressure across the interface of the fluid flow and the porous media has been studied and is well-known nowadays. The normal velocity is continuous, which leads to

$$\mathbf{u}_f \cdot \mathbf{n} = \mathbf{u}_D \cdot \mathbf{n}, \tag{3}$$

where again we assume that **n** is the unit normal direction at the interface pointing outward to the fluid side. The stress acting on the interface should be balanced which leads two more interface relations

$$[p] = 2\mu_f \mathbf{n} \cdot \mathbf{D}_f \cdot \mathbf{n}, \tag{4}$$

$$\frac{\alpha}{\sqrt{K}}(\mathbf{u}_f - \mathbf{u}_D) \cdot \boldsymbol{\tau} = 2\boldsymbol{\tau} \cdot \mathbf{D}_f \cdot \mathbf{n} \quad \text{or} \quad \frac{\alpha}{\sqrt{K}}\mathbf{u}_f \cdot \boldsymbol{\tau} = 2\boldsymbol{\tau} \cdot \mathbf{D}_f \cdot \mathbf{n}, \tag{5}$$

where $\mathbf{D}_f = \frac{1}{2}\left(\nabla \mathbf{u}_f + \nabla^T \mathbf{u}_f\right)$ is the deformation tensor, $\boldsymbol{\tau}$ is the unit tangent vector, and $\frac{\sqrt{K}}{\alpha}$ is the friction constant arising from the experimental data and dimensional analysis [25]. For convenience, we denote $K_2 = \frac{\alpha}{\sqrt{K}}$. The jump in the pressure is defined as $[p] = p_f - p_D$ and this definition will be applied to other variables throughout the paper. Thus we have $[\mathbf{u} \cdot \mathbf{n}] = 0$ and $[\nabla \cdot \mathbf{u}] = 0$. The second equation in (5) is so called the Beavers–Joseph–Saffman (BJS) condition while the first one is called the Beavers–Joseph (BJ) condition. Most numerical methods in the literature use the BJS equation as a valid approximation while our augmented approach can handle the more complicated tangential slip condition as shown in the first equation in (5) or non-homogeneous cases as shown in some of our numerical examples. In the remaining of the paper, for the sake of simplicity, we omit the subscripts f and D in notations of $\mathbf{u}_f$, $\mathbf{u}_D$, p_f and p_D if there is no confusion since the present coupled equations will be solved as one whole system.

Note that if we know $[\mathbf{u} \cdot \boldsymbol{\tau}]$ and $[\mathbf{u} \cdot \mathbf{n}]$ (which is zero according to the first interface condition), we can get the jump relations of the velocity for each component. At a point $\mathbf{X} = (X, Y)$ on the interface, let θ be the angle between the normal direction of the interface and the x-axis, see the diagram in Fig. 1. Then the unit normal direction is $\mathbf{n} = (\cos\theta, \sin\theta)$. If we define

$$[\mathbf{u} \cdot \boldsymbol{\tau}] = q_5, \tag{6}$$

and combine with $[\mathbf{u} \cdot \mathbf{n}] = 0$, we get

$$0 = [u]\cos\theta + [v]\sin\theta, \tag{7}$$

$$q_5 = -[u]\sin\theta + [v]\cos\theta. \tag{8}$$

By solving the jumps of $[u]$ and $[v]$ from the above system, we obtain

$$[u] = -q_5 \sin\theta, \qquad [v] = q_5 \cos\theta. \tag{9}$$

There are many applications of the interactions between a fluid flow and a porous media, which has attracted a lot of attentions in the literature. Earlier works have been focused on solving Stokes and Darcy coupling equations, particularly using finite elements or domain decomposition methods, see for example, [1–5,7–10,12,14–17,19,20,23–25,32–36] and the references therein. For the Navier–Stokes and Darcy coupling, theoretical analysis and numerical methods, particularly finite element methods have been catching up, see for example, [5,11,13,18] for an incomplete list and the reference therein.

In the above mentioned literature, almost all the numerical methods are based on finite element formulations or domain decomposition methods. In [27], an alternative approach based on a finite difference discretization and a Cartesian mesh was proposed for solving the Stokes and Darcy coupling. The idea of the approach is to transform the original coupling problem to three Poisson equations with a source and dipole distributions corresponding to the jumps in the solution and the normal derivative of the Poisson equations. Some augmented variables are introduced along the interface so that the solutions of the velocity and pressure satisfy original interface conditions as shown in Eqs. (3)–(5). One of advantages is that a fast Poisson solver can be utilized on the rectangular domain. The method produces second order accurate approximation for the velocity but *first* order accurate approximation for the pressure.

In this paper, we propose a Cartesian finite difference method to solve Navier–Stokes and Darcy coupling equations based on some of ideas in [27]. We first rewrite the Navier–Stokes equations in the fluid domain using the equivalent pressure Poisson equation formulation introduced by Johnston and Liu [21,22], and then also rewrite the Darcy's equations in the porous media domain by taking the divergence operator to the velocity field so that the coupling equations can be written as one whole system, see the details in next section. We attempted to use the augmented approach in [27] combined with a Navier–Stokes solver to simulate the Navier–Stokes and Darcy coupling problems. The attempt worked only for a few time steps before the computed solution either blows up or loses accuracy. After some careful analysis and numerical experiments, we came to the idea to enforce the divergence free condition at the interface from the fluid side as an extra augmented equation (constraint). Thus the resultant Schur complement matrix for the augmented variables in discretization is over-determined and the least squares solution is used for the coupling problem. That is why the new method is called the least squares augmented immersed interface method.

Below we briefly summarize the novelty of this paper.

- With this new least squares augmented IIM approach, we have developed a finite difference scheme to efficiently solve the

Navier–Stokes and Darcy coupling equations with second order accuracy both in the velocity and pressure.

- With the new method, we have obtained some interesting simulation results for time dependent problems that cannot be solved using the method in [27] for Stokes and Darcy coupling.

The method in this paper is different from that in [27] for Stokes and Darcy coupling equations not only for solving different couplings, but also in the methodology with the new idea in enforcing the divergence condition along the interface. In this paper, we also present some comparison results of the two approaches. For stationary Stokes and Darcy coupling equations, both methods can work. However, as the mesh gets finer, the five-equations method in [27] may be less accurate compared with that obtained from the new (six-equations) approach as the augmented variable may loose accuracy due to the larger condition number of the Schur complement.

The rest of the paper is organized as follows. In the next section, we explain the theoretical aspects of the least squares augmented method for the Navier–Stokes and Darcy coupling equations. The mathematical equivalence of the original and transformed problems will also be discussed. In Section 3, we introduce the time discretization for the transformed equations based on a variant of the pressure Poisson equation formulation and derive the resultant Schur complement matrix. Numerical accuracy check and the comparisons with previous method will be given in Section 2.2, while some interesting flow simulations with various shapes and orientations of the interface will be given in Section 5. Conclusions and acknowledgements are given in the last two sections.

2. The least squares augmented method for Navier–Stokes and darcy coupling equations

In this section, we explain the theoretical basis of the proposed numerical method. We transform the original governing equations (1) and (2) to an equivalent form so that we get several Poisson/Helmholtz equations that are easier to solver separately. Note that, the theoretical justification of the transform for the Navier–Stokes part is based on the pressure Poisson equation formulation discussed in [21,22]. By applying the divergence operator to the momentum equation of the Navier–Stokes equations and the Darcy's law, the entire problem can be re-written as

$$\Delta p = \begin{cases} \nabla \cdot \mathbf{F} - \rho \nabla \cdot (\mathbf{u} \cdot \nabla \mathbf{u}), & \mathbf{x} \in \Omega_f, \\ 0, & \mathbf{x} \in \Omega_D, \end{cases} \tag{10}$$

$$[p] = q_1, \qquad [p_n] = q_2, \qquad \text{on } \Gamma;$$

$$\Delta u = \begin{cases} \dfrac{1}{\mu}\left(p_x - F_1 + \rho\left(\dfrac{\partial u}{\partial t} + \mathbf{u} \cdot \nabla u\right)\right), & \mathbf{x} \in \Omega_f, \\ -K_1 \Delta p_x, & \mathbf{x} \in \Omega_D, \end{cases} \tag{11}$$

$$[u] = -q_5 \sin\theta, \qquad [u_n] = q_3, \qquad \text{on } \Gamma;$$

$$\Delta v = \begin{cases} \dfrac{1}{\mu}\left(p_y - F_2 + \rho\left(\dfrac{\partial v}{\partial t} + \mathbf{u} \cdot \nabla v\right)\right), & \mathbf{x} \in \Omega_f, \\ -K_1 \Delta p_y, & \mathbf{x} \in \Omega_D, \end{cases} \tag{12}$$

$$[v] = q_5 \cos\theta, \qquad [v_n] = q_4, \qquad \text{on } \Gamma,$$
$$\nabla \cdot \mathbf{u} = 0, \tag{13}$$

where $p_n = \nabla p \cdot \mathbf{n} = \dfrac{\partial p}{\partial n}$ is the normal derivative of p and $[p_n] = \dfrac{\partial p_f}{\partial n} - \dfrac{\partial p_D}{\partial n}$. Similar definitions are applied to $[u_n]$ and $[v_n]$. Here,

$q_1, ..., q_5$ are introduced augmented variables along the interface Γ. The augmented variables are part of unknowns with co-dimension one whose solutions satisfy the interface conditions (3)–(5). In the Darcy's region, we also have the Darcy's law

$$u_D = -K_1 \frac{\partial p_D}{\partial x}, \qquad v_D = -K_1 \frac{\partial p_D}{\partial y}, \tag{14}$$

in addition to $\nabla \cdot \mathbf{u}_D = 0$. In this way, we decouple the original problem to three separated Helmholtz/Poisson equations literately and an explicit expression (14). Note that from above equations, we cannot conclude $\nabla \cdot \mathbf{u}_f = 0$ until it is true along the interface and the boundary from the fluid side. That is the starting point of the new method.

2.1. Augmented equations

The above Navier–Stokes and Darcy governing equations are coupled by *six* interface conditions along the interface Γ,

$$[p] = 2\mu \, \mathbf{n} \cdot \mathbf{D}_f \cdot \mathbf{n}, \tag{15}$$

$$K_2 \left(\mathbf{u}_f - \mathbf{u}_D\right) \cdot \boldsymbol{\tau} = 2\, \boldsymbol{\tau} \cdot \mathbf{D}_f \cdot \mathbf{n}, \quad \text{or} \quad K_2 \mathbf{u}_f \cdot \boldsymbol{\tau} = 2\, \boldsymbol{\tau} \cdot \mathbf{D}_f \cdot \mathbf{n}, \tag{16}$$

$$\frac{\partial p_f}{\partial n} = \mu \Delta \mathbf{u}_f \cdot \mathbf{n} + \left(\mathbf{F} - \rho\left(\frac{\partial \mathbf{u}_f}{\partial t} + \mathbf{u}_f \cdot \nabla \mathbf{u}_f\right)\right) \cdot \mathbf{n}, \tag{17}$$

$$\frac{\partial p_D}{\partial n} = -\frac{1}{K_1}\left(\mathbf{u}_D \cdot \mathbf{n}\right), \tag{18}$$

$$[\mathbf{u} \cdot \boldsymbol{\tau}] = q_5, \tag{19}$$

$$\nabla \cdot \mathbf{u}_f = 0. \tag{20}$$

The first five equations are similar to those for the Stokes and Darcy coupling described in [27]. However, we impose extra augmented equation (20) on the interface. Since there are only five augmented variables $q_1, ..., q_5$, in discretization, we would have more equations than unknowns. That is why the new method is called the least squares augmented method.

2.2. Equivalence of the original and transformed governing equations

The well-posedness of the Stokes and Darcy; and the Navier–Stokes and Darcy coupling has been well addressed in the literature, for example, [25]. Assume that the original models are well-posed with suitable regularity in each sub-domain; that is, the solutions exist and are unique except for the pressure up to a constant. Then the solutions to the transformed problem Eqs. (10)–(14) with augmented Eqs. (15)–(20) also exist since they are all defined from original variables and satisfy the transformed equations which are exactly derived from the original governing equations. In other words, the solutions to the original problem are also solutions to the transformed problem if the regularity conditions are satisfied in each sub-domain. More precisely, let u and v, and p be the solution to the original problem. From these quantities, we define $q_1 = [p]$, $q_2 = [p_n], \ldots, q_5 = [\mathbf{u}] \cdot \boldsymbol{\tau}$ according to (10)–(13). From the definitions of u and v, p, and $q_1, \ldots, q_5$, they satisfy the transformed Eqs. (10)–(14) and augmented Eqs. (15)–(20). Thus the existence of the solutions to the transformed systems has been established.

The uniqueness of the solution is more subtle. The issue has been addressed to some extent for the Stokes and Darcy coupling in [27]. The key is whether the incompressibility condition is satisfied up to the boundary. The argument in [27] is that the incompressibility condition along the boundary/inteface is redundant at least numerically and therefore can be discarded. Theoretically, it

is still an open question that the velocity of the transformed system is divergence free. In our new approach, we simply enforce the divergence free condition along the interface for the transformed equations. Thus the solution to the transformed system is also a solution to the original problem since all original equations now are satisfied. The sensitivity of new formulation still needs to be investigated.

3. The algorithm for the Navier–Stokes and Darcy coupling

In this section, we explain the method for the Navier–Stokes and Darcy coupling. The Navier–Stokes solver is the one based on the pressure Poisson equation formulation developed in [21,22,31]. The algorithm is described in detail in this section.

We assume the entire computational domain $\Omega = \Omega_f \cup \Omega_D$ is a rectangle $[a, b] \times [c, d]$. We use a uniform grid,

$$x_i = a + ih_x, \quad i = 0, 1, \ldots M, \quad h_x = \frac{b-a}{M}; \tag{21}$$

$$y_j = c + jh_y, \quad j = 0, 1, \ldots N, \quad h_y = \frac{d-c}{N}, \tag{22}$$

where the velocity and pressure are all defined at the collocated grid points (x_i, y_j). Note that, it is possible to use the MAC (mark-and-cell) grid, which usually provides better results and does not require the boundary condition for the pressure. However, the presence of an arbitrary interface would make the programming much more complicated when using the MAC grid. In our numerical experiments shown in later sections, we do not encounter any stability issue when we use the collocated grid since the Reynolds number considered here is modest. The augmented equations at the interface and the boundary also make numerical schemes more stable. The interface between the flow and porous media is discretized by a set of control points $(X_l, Y_l), l = 1, 2 \ldots N_b$ connected by a cubic spline [28]. The jump and interface conditions, and the augmented variables are all defined at those control points in the discretization. We use a time marching scheme to obtain approximate solutions at different time level t^k with a known initial condition at $t^0 = 0$. Here the time step size is a constant for simplicity although we can use an adaptive one. From time step t^k to $t^{k+1} = t^k + \Delta t$, we denote the discrete solution (approximation to p, u, and v) at time step t^k as $\{P_{ij}^k\}$, $\{U_{ij}^k\}$, and $\{V_{ij}^k\}$ which together form a vector $\tilde{\boldsymbol{u}}^k$ with dimension $O(3MN)$, where M and N are the number of grid lines in the x- and y-directions, respectively. We also denote the discrete solution (approximation to q_1, q_2, ..., q_5) at time step t^k as $Q_{1,l}^k$, $Q_{2,l}^k$, ..., $Q_{5,l}^k$, $l = 1, 2, \ldots, N_b$, which together to form a vector $\mathbf{Q}^k \in R^{5N_b}$.

3.1. Time marching scheme from time t^k to t^{k+1}.

Assume that we have already computed the velocity (U_{ij}^k, V_{ij}^k), the pressure P_{ij}^k, at time level k, we use the Crank–Nicholson type discretization and the augmented idea to compute the solutions at the next time level t^{k+1}.

Given an augmented vector $\mathbf{Q}^{k+1}$, we solve the pressure in Eq. (10) using the IIM to get $\{P_{ij}^{k+1}\}$ from the following,

$$\Delta p^{k+1} = \begin{cases} \nabla \cdot \mathbf{F}^{k+1/2} - \rho \nabla \cdot (\mathbf{u} \cdot \nabla \mathbf{u})^{k+1/2}, & \mathbf{x} \in \Omega_f, \\ 0 & \mathbf{x} \in \Omega_D, \end{cases} \tag{23}$$

$$[p^{k+1}] = q_1^{k+1}, \qquad \left[\frac{\partial p^{k+1}}{\partial n}\right] = q_2^{k+1}, \qquad \text{on } \Gamma. \tag{24}$$

In the expressions above, we use a second order Adams-Bashforth scheme to approximate the non-linear term as

$$\nabla \cdot (\mathbf{u} \cdot \nabla \mathbf{u})^{k+1/2} = \frac{3}{2} \nabla \cdot (\mathbf{u} \cdot \nabla \mathbf{u})^k - \frac{1}{2} \nabla \cdot (\mathbf{u} \cdot \nabla \mathbf{u})^{k-1}. \tag{25}$$

Once we obtain the pressure, we can solve the Helmholtz equations (11)–(13) to get the predicted velocity from the following,

$$\Delta u^* - \frac{2\rho}{\mu \Delta t} u^* = \begin{cases} \frac{2}{\mu}\left(p_x^{k+1} - \frac{\rho}{\Delta t} u^k\right) - \Delta u^k \\ + \frac{2}{\mu}\left(\rho(\mathbf{u} \cdot \nabla u)^{k+1/2} - F_1^{k+1/2}\right), & \mathbf{x} \in \Omega_f, \\ -K_1 \Delta p_x^{k+1} + \frac{2K_1\rho}{\mu \Delta t} p_x^{k+1}, & \mathbf{x} \in \Omega_D, \end{cases} \tag{26}$$

$$[u^*] = -q_5^{k+1} \sin\theta, \qquad \left[\frac{\partial u^*}{\partial n}\right] = q_3^{k+1}, \qquad \text{on } \Gamma;$$

$$\Delta v^* - \frac{2\rho}{\mu \Delta t} v^* = \begin{cases} \frac{2}{\mu}\left(p_y^{k+1} - \frac{\rho}{\Delta t} v^k\right) - \Delta v^k \\ + \frac{2}{\mu}\left(\rho(\mathbf{u} \cdot \nabla v)^{k+1/2} - F_2^{k+1/2}\right), & \mathbf{x} \in \Omega_f, \\ -K_1 \Delta p_y^{k+1} + \frac{2K_1\rho}{\mu \Delta t} p_y^{k+1}, & \mathbf{x} \in \Omega_D, \end{cases} \tag{27}$$

$$[v^*] = -q_5^{k+1} \cos\theta, \qquad \left[\frac{\partial v^*}{\partial n}\right] = q_4^{k+1}, \qquad \text{on } \Gamma;$$

Note that in the Darcy's region, we add the term $-\frac{2\rho}{\mu \Delta t}\mathbf{u}^*$ to the left so that the right hand side becomes $\frac{2K_1\rho}{\mu \Delta t}\nabla p^{k+1}$ (since $\mathbf{u} = -K_1\nabla p$). Thus, the intermediate velocity can be solved by a fast Helmholtz solver in the entire rectangular domain[1]

Finally, we can proceed with the projection step to ensure the divergence free condition for the computed velocity,

$$\begin{cases} \Delta \psi^{k+1} = \frac{\nabla \cdot \mathbf{u}^*}{\Delta t}, & \mathbf{x} \in \Omega \\ \left.\frac{\partial \psi^{k+1}}{\partial n}\right|_{\partial \Omega} = 0, \quad [\psi^{k+1}] = 0, \quad \left[\frac{\partial \psi^{k+1}}{\partial n}\right] = 0, & \text{on } \Gamma; \end{cases} \tag{28}$$

$$\mathbf{u}^{k+1} = \mathbf{u}^* - \Delta t \nabla \psi^{k+1}. \tag{29}$$

Although we have the updated velocity in the whole domain Ω, we still replace the velocity by the Darcy's law in Ω_D as

$$u_D^{k+1} = -K_1 \frac{\partial p_D^{k+1}}{\partial x}, \qquad v_D^{k+1} = -K_1 \frac{\partial p_D^{k+1}}{\partial y}, \tag{30}$$

so that the Darcy's law can be exactly satisfied. The previous step is to make use of a fast Helmholtz solver for the velocity in the fluid region. The discretization of the first and second order derivatives involved above is based on the standard centered five-point finite difference formulas.

3.2. Augmented variables and the Schur complement matrix

The solutions to the *three* Poisson/Helmholtz equations (23)–(27) with jumps in the solution and the normal derivative in the matrix-vector form can be written as

$$A \tilde{\boldsymbol{u}}^{k+1} + B\mathbf{Q}^{k+1} = \tilde{\mathbf{F}}_1^{k+1} \tag{31}$$

---

[1] A direct application of IIM will lead to $O(1)$ local truncation errors near the interface because of $O(h/\Delta t) = O(1)$, and thus a first order accurate solution globally.

for some vector $\tilde{\mathbf{F}}_1^{k+1}$ and sparse matrices A and B.

The next step is to evaluate the residual of the augmented equations (15)–(20). This step involves local interpolations and it is equivalent to discretize the interface conditions (15)–(20).

At each control point $\mathbf{X}_l$, we interpolate the discrete solution $\{P_{ij}^{k+1}\}$, $\{U_{ij}^{k+1}\}$, and $\{V_{ij}^{k+1}\}$ to get their values, normal and tangential derivatives from each side of the interface, $P_l^{k+1,\pm}$, $(\frac{\partial P}{\partial n})_l^{k+1,\pm}$, $(\frac{\partial P}{\partial \tau})_l^{k+1,\pm}$ and so on. Note that, for a Poisson/Helmholtz equation with known jump conditions in the solution and the normal derivative, the computed solution and first order partial derivatives at grid points have been proved to be second order accurate using the IIM [6]. From the second order accurate values at grid points, we also get second order accurate values at the control points since the coefficients of the interpolations are $O(1)$.

The discretization of the interface conditions (15)–(20) can be formally written as

$$R(\mathbf{Q}^{k+1}) = C\tilde{\boldsymbol{u}}^{k+1} + D\mathbf{Q}^{k+1} - \tilde{\mathbf{F}}_2^{k+1} \tag{32}$$

for some sparse matrices C and D. The solution $(\tilde{\boldsymbol{u}}^{k+1}, \mathbf{Q}^{k+1})$ satisfies $R(\mathbf{Q}^{k+1}) = \mathbf{0}$ and Eq. (31) so we have the following system of equations,

$$\begin{bmatrix} A & B \\ C & D \end{bmatrix} \begin{bmatrix} \tilde{\boldsymbol{u}}^{k+1} \\ \mathbf{Q}^{k+1} \end{bmatrix} = \begin{bmatrix} \tilde{\mathbf{F}}_1^{k+1} \\ \tilde{\mathbf{F}}_2^{k+1} \end{bmatrix}. \tag{33}$$

Therefore, the Schur complement for $\mathbf{Q}^{k+1}$ is

$$(D - CA^{-1}B)\mathbf{Q}^{k+1} = \tilde{\mathbf{F}}_2^{k+1} - CA^{-1}\tilde{\mathbf{F}}_1^{k+1} = \bar{\mathbf{F}}^{k+1}, \quad \text{or}$$
$$S\mathbf{Q}^{k+1} = \bar{\mathbf{F}}^{k+1}. \tag{34}$$

It has been shown in [29] and other related papers, that the matrix-vector multiplication $S\mathbf{Q}^{k+1}$ given $\mathbf{Q}^{k+1}$ is simply

$$S\mathbf{Q}^{k+1} = R(\mathbf{Q}^{k+1}) + \bar{\mathbf{F}}^{k+1} = R(\mathbf{Q}^{k+1}) - R(\mathbf{0}), \tag{35}$$

where $R(\mathbf{Q}^{k+1}) = S\mathbf{Q}^{k+1} - \bar{\mathbf{F}}^{k+1}$. The right hand side of $S\mathbf{Q}^{k+1} = \bar{\mathbf{F}}^{k+1}$ can be computed from $-R(\mathbf{0})$ corresponding to the residual of the interface conditions with zero value of augmented variables which results from the three regular Poisson/Helmholtz equations on the rectangular domain. In our numerical tests, we form the matrix S, but not A, B, C, and D, by using $\mathbf{Q}^{k+1} = \mathbf{e}_i$, $i = 1, 2, \ldots, 5N_b$. The coefficient matrix has a rectangular form with the dimension of $6N_b \times 5N_b$. We then use the singular value decomposition (SVD) to find the least squares solution of the system. We outline the numerical algorithm from time step t^k to t^{k+1} as follows.

Step 1: Find the right hand side of the Schur complement $\bar{\mathbf{F}}^{k+1}$ by setting $\mathbf{Q}^{k+1} = \mathbf{0}$, solving the transformed problem (10)–(14) to get $\tilde{\boldsymbol{u}}^{k+1}(\mathbf{0})$, and using $\tilde{\boldsymbol{u}}^{k+1}(\mathbf{0})$ and $\mathbf{Q}^{k+1} = \mathbf{0}$ to interpolate interface quantities needed in Eqs. (15)–(20). The residual of the interface conditions is the right hand side of the Schur complement with a negative sign.

Step 2: For $i = 1, 2, \ldots, 5N_b$, we set $\mathbf{Q}^{k+1} = \mathbf{e}_i$, the i-th unit vector, solve the transformed problem (10)–(14) to get $\tilde{\boldsymbol{u}}^{k+1}(\mathbf{Q})$, and then interpolate $\tilde{\boldsymbol{u}}^{k+1}(\mathbf{Q})$ to get the residual of the interface conditions (15)–(20). The i-th column of the Schur complement is the residual of the interface conditions (15)–(19) plus the right hand side $\bar{\mathbf{F}}^{k+1}$. Note that, for a fixed interface and constant time step size, this step just needs to be done once initially.

Step 3: Solve the Schur complement system to get the solution $\mathbf{Q}^{k+1}$ using the SVD decomposition.

Step 4: Solve the transformed problem (10)–(14) with computed $\mathbf{Q}^{k+1}$ to get the pressure and velocity $\tilde{\boldsymbol{u}}^{k+1}$.

3.3. Some implementation details

There are some major differences between the algorithm for solving the Navier–Stokes and Darcy coupling and that for the Stokes and Darcy coupling. We outline a few as below.

For the Stokes and Darcy coupling, we need to solve three Poisson equations. For the Navier–Stokes and Darcy coupling, we need to solve a Poisson equation for the pressure, but two Helmholtz equations for the predicted velocity $\mathbf{u}^*$. The coefficient $-\frac{2\rho}{\mu\Delta t}$ is of $1/\Delta t \sim 1/h$ in the Navier–Stokes equations but it should be zero for the Darcy's equation. This $O(1/h)$ jump in the coefficient of the $\mathbf{u}^*$ term in the Helmholtz equations would lead to $O(h)$ error in the solution, see for example, [26,29]. However, there is no such issue for the Stokes and Darcy coupling. In present approach, we add the term $-\frac{2\rho}{\mu\Delta t}\mathbf{u}^*$ to both sides of the Darcy's equation. In this way, we can get rid of the discontinuity in the coefficient, and still are able to use the fast Helmholtz solver in the entire rectangular domain. The value of $\mathbf{u}^*$ in the Darcy's region is just a ghost value to make the computation in the whole domain more accurate and efficient. After $\mathbf{u}^*$ in the flow region has been computed, we replace the value in Darcy's region by $\mathbf{u}^{k+1} = -K_1 \nabla p^{k+1}$.

Using the pressure Poisson equation formulation, how to compute $\Delta \mathbf{u} \cdot \mathbf{n}$ along the boundary $\partial\Omega$ and the interface Γ is crucial to the stability of the algorithm. A direct interpolation from $\mathbf{u}$ to get $\Delta \mathbf{u}$ often leads to instability. There are a few discussions in the literature about how to compute $\Delta \mathbf{u} \cdot \mathbf{n}$ if the velocity is known along rectangular boundaries, see for example, [21,30]. It is quite challenging for curved boundaries/interfaces and different boundary/interface conditions. We use the relation

$$\mu\Delta\mathbf{u}_f = \rho\left(\frac{\partial \mathbf{u}_f}{\partial t} + \mathbf{u}_f \cdot \nabla\mathbf{u}_f\right) + \nabla p_f - \mathbf{F}_f \tag{36}$$

to get the value of $\Delta\mathbf{u}_f$ at grid points, then interpolate them to get the values at the control points needed for the augmented equations. Note that the right hand side only involves first order derivatives of those fluid quantities.

Again, using the pressure Poisson equation formulation, it has been discussed in the literature that it is not necessary to perform the projection step. We have tested both approaches with and without the projection step. The method with the projection gives better results even though not significantly. Furthermore, the enforcement of the incompressibility condition would ensure the equivalence of the original and transformed problems as discussed earlier. Note that, for fixed interfaces and time independent interface conditions (15)–(20), the Schur complement matrix S is a fixed time-independent matrix so the SVD decomposition just needs to be performed once.

4. Numerical accuracy tests and comparisons

In this section, we show some numerical accuracy tests for the present algorithm and the comparison with previous one in [27]. We use a uniform mesh with $h_x = h_y = h = 4/N$ for various N so that we can utilize a fast Poisson/Helmholtz solver. The computational domain is $[-2, 2] \times [-2, 2]$. The interface is expressed using the cubic spline package [28]. Throughout this section, the interface Γ is a unit circle $x^2 + y^2 = 1$ and all physical parameters such as ρ, μ, K_1, K_2 are all set to be one for simplicity, unless otherwise stated. The errors of the computed solutions are defined in L^∞ norm as

$$\|E_p\|_\infty^N = \max_{i,j} \left| p(x_i, y_j, T) - P_{ij}^K \right|, \tag{37}$$

$$\|E_\mathbf{u}\|_\infty^N = \max_{i,j} \sqrt{\left(u(x_i, y_j, T) - U_{ij}^K\right)^2 + \left(v(x_i, y_j, T) - V_{ij}^K\right)^2}, \tag{38}$$

(a)

μ=1, K=0.02, u=1, time=6.5

(b)

μ=1, K=0.02, u=1, time=6.5

(c)

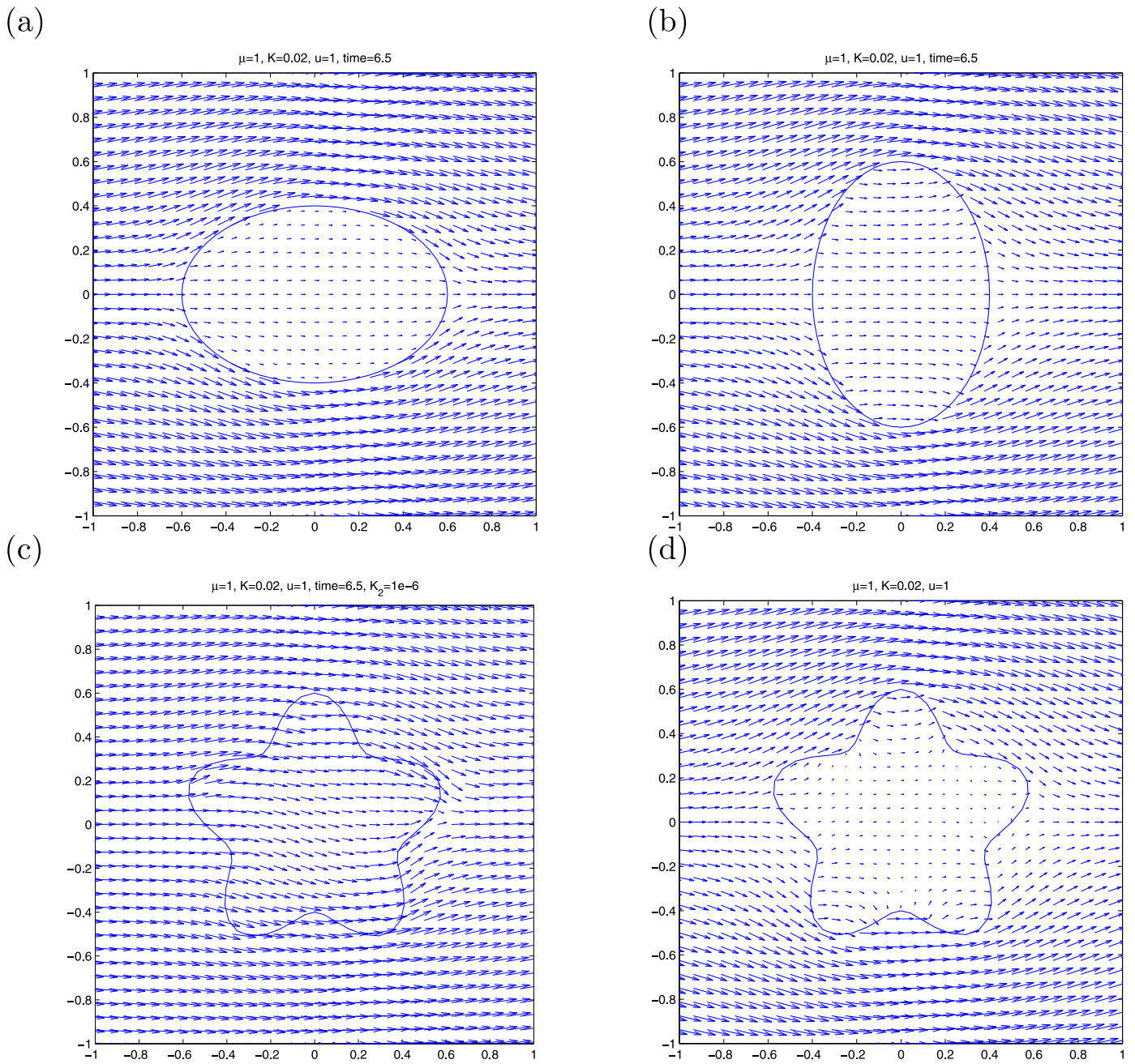μ=1, K=0.02, u=1, time=6.5, K₂=1e−6

(d)

μ=1, K=0.02, u=1

Fig. 2. Velocity plot of a fluid flow and a porous media (inside the domain) modeled by the Navier–Stokes and Darcy coupling. (a) and (b), the interfaces are ellipses. (c) and (d), the interface is $r = 0.5 + 0.1 \sin 5\theta$ in the polar coordinates. For smaller K's, the porous media acts as some sort of obstacles while for larger ones, the flow can go through easily. In all the simulations, the final time is $T = 6.5$. The inflow condition is $u = 1$, $v = 0$. $K = K_1$.

for a mesh size N by N, where K is the final time step corresponding to the final time $T = K\Delta t$. The order of accuracy is given approximately by

$$order = \log_2 \left(\|E_p\|_\infty^N / \|E_p\|_\infty^{2N} \right) \tag{39}$$

for the pressure and similarly for the velocity. Unless otherwise stated, we choose the number of control points $N_b = N$.

4.1. Accuracy check against analytic solutions

To validate our numerical algorithm, we first compare the computed solutions against analytic solutions. The first example has a discontinuous tangential slip for the velocity field while the pressure is continuous along the interface Γ. The normal derivative of the pressure is also discontinuous across the interface. On the other hand, the second example has a continuous tangential velocity but the pressure is discontinuous along the interface. The normal derivatives of the velocity components are also discontinuous across the interface. The discontinuities are varying along the interface in the second example. Notice that, both examples have continuous normal velocity along the interface since it is one of the required interface conditions as discussed earlier. We demonstrate that our present algorithm can handle both cases well so more general examples can work without any difficulty.
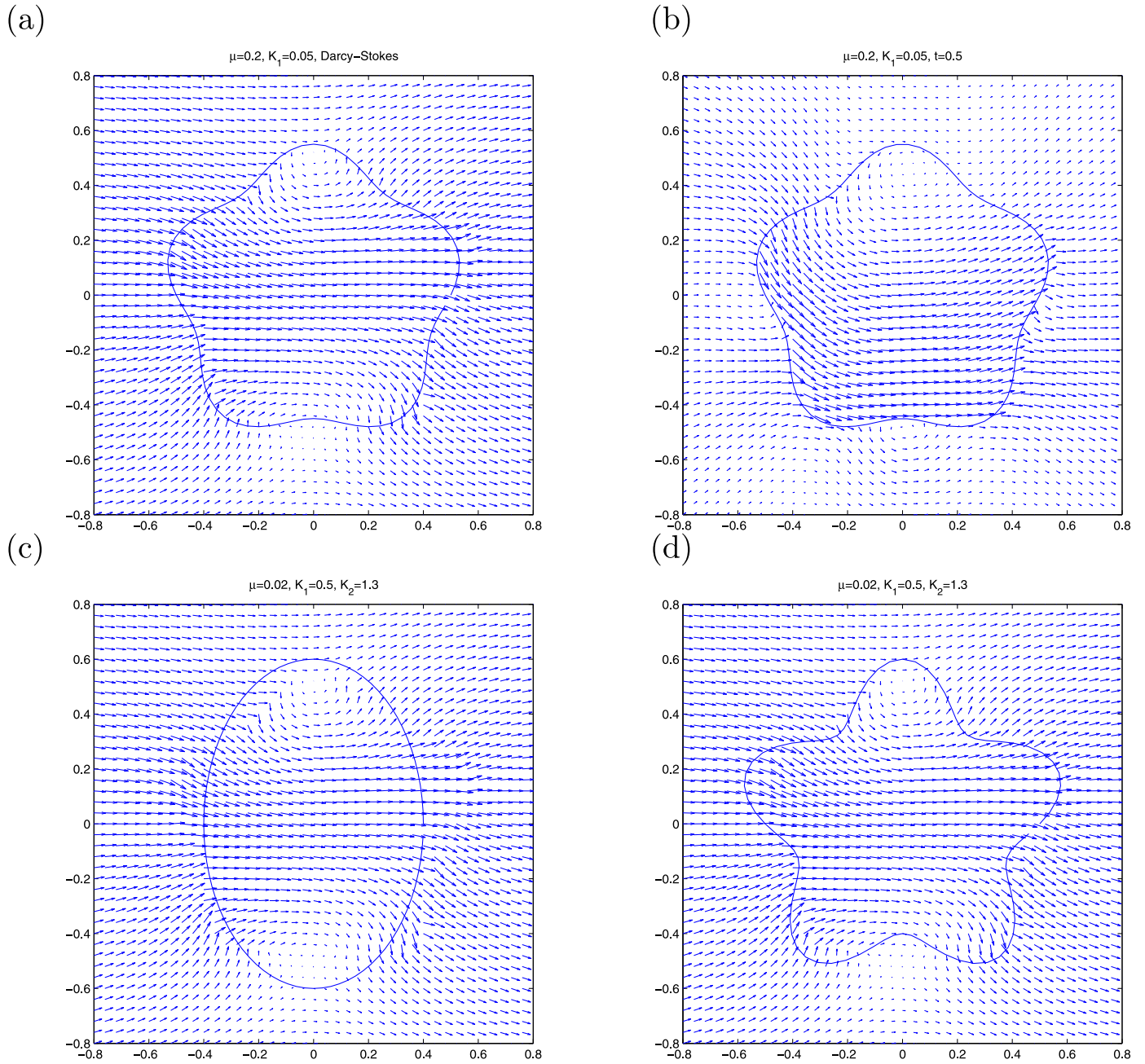
(a)

$\mu=0.2$, $K_1=0.05$, Darcy–Stokes

(b)

$\mu=0.2$, $K_1=0.05$, t=0.5

(c)

$\mu=0.02$, $K_1=0.5$, $K_2=1.3$

(d)

$\mu=0.02$, $K_1=0.5$, $K_2=1.3$

Fig. 3. Velocity plot of a porous media and a fluid flow (inside the domain) modeled by (a) the Darcy and Stokes coupling; and (b) the Darcy and Navier–Stokes coupling. The parameters are $\mu=0.2$, $K_1=0.05$, $K_2=1.3$ with the mesh $N=100$ and $N_b=80$. The interface is $r=0.5+0.1\sin 5\theta$ in the polar coordinates; (c)–(d) simulation results for the Darcy and Navier–Stokes coupling with the interfaces, $x^2/0.4^2+y^2/0.6^2=1$ and $r=0.5+0.2\sin 5\theta$, respectively. The parameters are set as $\mu=0.02$, $K_1=0.5$, and $K_2=1.3$. The initial data is obtained using the solution of the Darcy and Stokes coupling.

4.1.1. Example 1

The analytic solution of the Navier–Stokes equations is

$$u_f = g(t)\Big(y(x^2+y^2-1)+2y\Big),$$

$$v_f = g(t)\Big(-x(x^2+y^2-1)-2x\Big),$$

$$p_f = g(t)\Big(x^2+y^2\Big), \tag{40}$$

defined outside of the unit circle $x^2+y^2=1$ while the analytic solution for the Darcy's system is $u_D=v_D=0$, and $p_D=g(t)$. At the interface $x^2+y^2=1$, we have

$$\mathbf{n}=[x,\,y]^T, \quad \boldsymbol{\tau}=[-y,\,x]^T, \quad p_f=g(t), \quad p_D=g(t),$$

$$u_f = 2y\,g(t), \quad v_f = -2x\,g(t),$$

$$u_D = 0, \quad v_D = 0, \quad \frac{\partial u_f}{\partial n} = 4y\,g(t), \quad \frac{\partial v_f}{\partial n} = -4x\,g(t),$$

$$\frac{\partial u_f}{\partial \tau} = 2x\,g(t), \quad \frac{\partial v_f}{\partial \tau} = 2y\,g(t),$$

$$\mathbf{n}\cdot\mathbf{D}_f\cdot\mathbf{n} = 0 \qquad \boldsymbol{\tau}\cdot\mathbf{D}_f\cdot\mathbf{n} = 0. \tag{41}$$

It is easy to check that the above solutions $\mathbf{u}_f$ and $\mathbf{u}_D$ satisfy the Navier–Stokes and Darcy's equations, respectively, with the source term $\mathbf{F}$ in the Navier–Stokes equations being computed directly from the analytic solution. The interface condition (4), $[p]=2\mu\,\mathbf{n}\cdot\mathbf{D}_f\cdot\mathbf{n}$ with $\mu=1$ is satisfied. The BJS condition (the second interface condition in Eq. (5)) is also satisfied. However, the solution
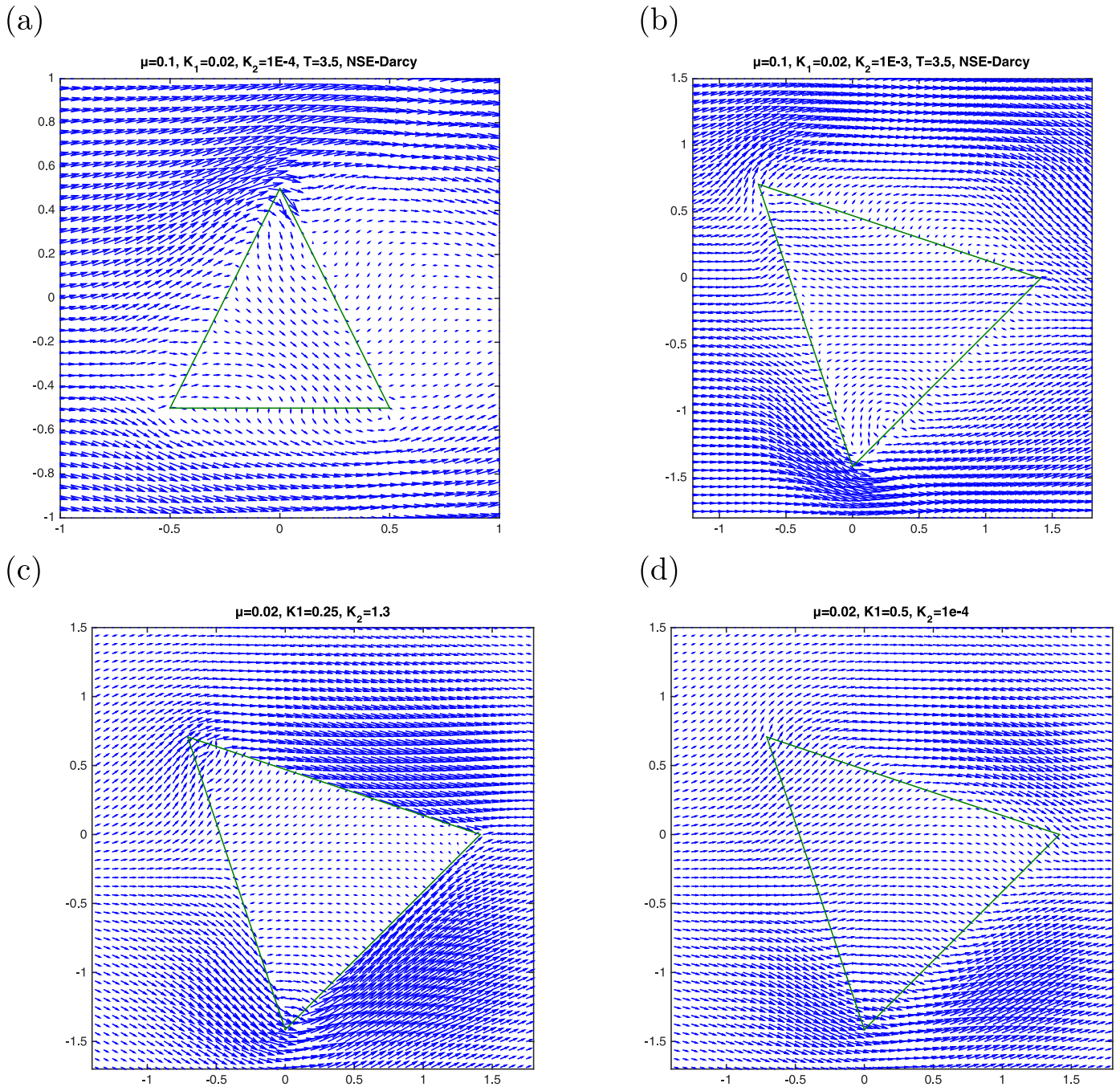
(a)

(b)

(c)

(d)

Fig. 4. Navier–Stokes and Darcy coupling with a sharp angled interface with different parameters at $T = 3.5$. In (a)-(b), the fluid flow is outside and the Darcy's law is inside of the interface; while in (c)-(d), the fluid flow is inside while the Darcy's law is outside of the interface. The parameters are $\mu = 0.1$, $K_1 = 0.02$, and $K_2 = 10^{-4}$ in (a); $\mu = 0.1$, $K_1 = 0.02$, and $K_2 = 10^{-3}$ in (b); $\mu = 0.02$, $K_1 = 0.25$, and $K_2 = 1.3$ in (c); and $\mu = 0.02$, $K_1 = 0.5$, and $K_2 = 10^{-4}$ in (d). The corners do have significant influences on the flow patterns.

does not satisfy the first condition (BJ) in Eq. (5) since $\boldsymbol{\tau} \cdot \mathbf{D}_f \cdot \mathbf{n} = 0$ while $-(\mathbf{u}_f - \mathbf{u}_D) \cdot \boldsymbol{\tau} = 2g(t)$. Nevertheless, the present algorithm can deal with either interface conditions in Eq. (5).

In Table 1, we show a grid refinement analysis for $g(t) = \sin t$ at the final time $T = 5$. In the table, the first column is the mesh size in both x- and y- directions; the second, fourth columns are the maximum errors of the pressure and velocity, while the third and fifth columns are corresponding order of accuracy, respectively. The sixth and seventh columns are the condition numbers of the Schur complement matrix defined as $cond(S) = \frac{\max_i \sigma_i}{\min_i \sigma_i}$, where σ_i are non-zero singular values of the Schur complement matrix, with

and without the augmented equation $\nabla \cdot \mathbf{u}_f|_\Gamma = 0$ along the interface, respectively. One can observe that the condition number with the constraint is significant smaller than that of without it, which would also affect the accuracy for the computed velocity and the pressure. In Table 1(a), we have the same number of control points on the interface as the mesh size, that is, $N_b = N$. The average orders for the pressure and velocity are 2.0231 and 3.2327, respectively. With the cubic spline representation of the interface, we can use fewer control points without affecting the accuracy for the pressure and the velocity. For an interface with a modest curvature, our cubic spline package has order of accuracy $O(h_s^3)$, where
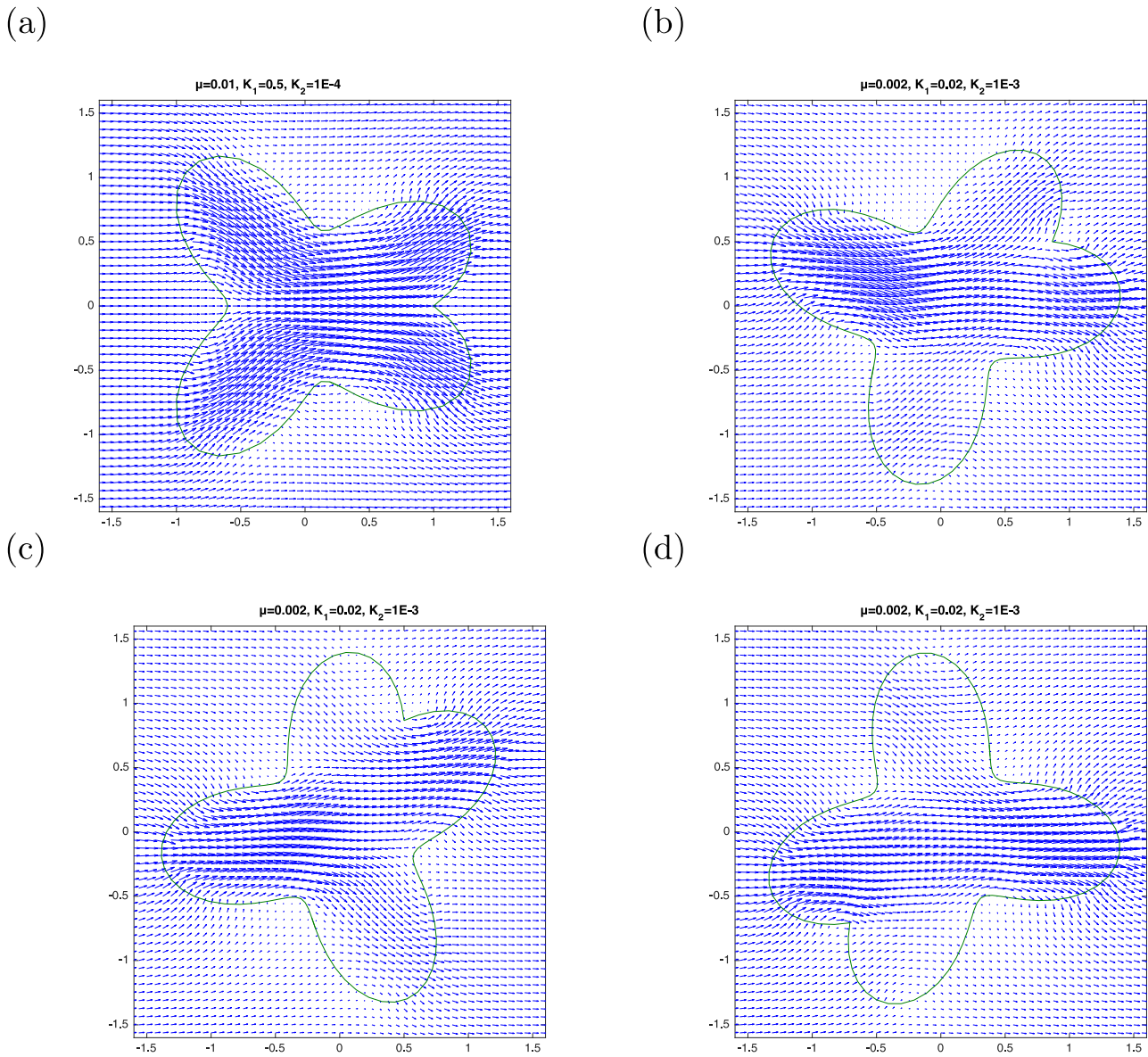
(a)

(b)

(c)

(d)

Fig. 5. Darcy and Navier–Stokes coupling with an interface and various parameters and different locations of the interface. The Darcy's law is defined outside of the interface. (a), $\mu = 0.1$, $K_1 = 0.5$, $K_2 = 10^{-4}$. (b), $\mu = 0.002$, $K_1 = 0.02$, $K_2 = 10^{-3}$. The interface is rotated counterclockwise by $\pi/6$. (c), $\mu = 0.002$, $K_1 = 0.02$, $K_2 = 10^{-3}$. The interface is rotated by $\pi/3$ counterclockwise. (d), $\mu = 0.002$, $K_1 = 0.02$, $K_2 = 10^{-3}$. The interface is rotated by $3\pi/4$ clockwise.

Table 1

A grid refinement analysis of Example 1 at time $T = 5$. The parameters are $\mu = 1$, $\rho = 1$, $K_1 = 1$, $K_2 = 1$. (a) the results with $N_b = N$. (b) the results with fewer control points $N_b < N$. The CPU times are 0.5462, 1.5884, 5.9216, 34.272, 226.9478 s for (b), respectively.

(a) The average order of accuracy for the pressure and velocity are 2.0231 and 3.2327, respectively. ($N_b = N$)

N	$\|E_p\|_\infty^N$	order	$\|E_u\|_\infty^N$	order	cond-6eq	cond-5eq
16	1.8890		$1.9839e-01$		$8.0806e+01$	$1.2104e+02$
32	$5.6152e-01$	1.7502	$2.1319e-02$	3.2182	$2.9443e+02$	$1.3904e+03$
64	$1.4805e-01$	1.9232	$1.7205e-03$	3.6313	$1.0435e+03$	$1.7704e+04$
128	$3.5373e-02$	2.0654	$1.4974e-04$	3.5223	$7.0632e+03$	$3.6746e+05$
256	$6.9209e-03$	2.3536	$2.5414e-05$	2.5588	$7.0651e+04$	$1.2520e+07$

(b) The average order of accuracy for the pressure and velocity are 2.0221 and 3.2110, respectively. ($N_b < N$)

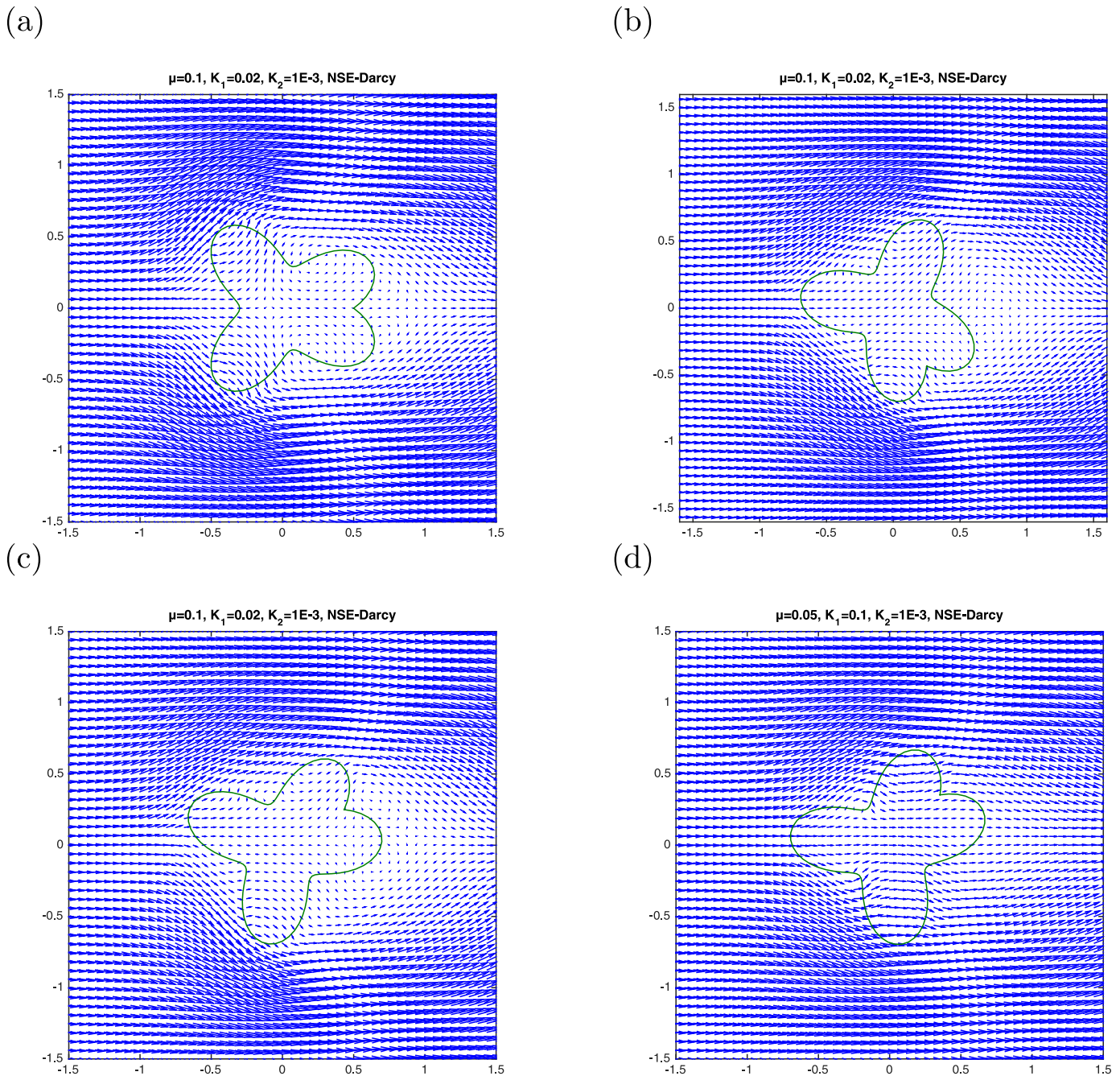| N	N_b	$\|E_p\|_\infty^N$	order	$\|E_u\|_\infty^N$	order	cond-6eq	cond-5eq
16	16	$1.8890e-00$		$1.9839e-01$		$8.0806e+01$	$1.2104e+02$
32	22	$5.7256e-01$	1.7221	$2.2640e-02$	3.1314	$2.0234e+02$	$7.3228e+02$
64	30	$1.4790e-01$	1.9528	$1.7365e-03$	3.7046	$7.7313e+02$	$6.7254e+03$
128	42	$3.5359e-02$	2.0645	$1.5333e-04$	3.5015	$3.0480e+03$	$8.4892e+04$
256	68	$6.9394e-03$	2.3492	$2.6986e-05$	2.5064	$1.0844e+04$	$1.0888e+06$

Fig. 6. Navier–Stokes and Darcy coupling with an interface and various parameters and different locations of the interface. The Darcy law is defined inside of the interface. (a), $\mu = 0.1$, $K_1 = 0.02$, $K_2 = 10^{-3}$. (b). $\mu = 0.1$, $K_1 = 0.02$, $K_2 = 10^{-3}$. The interface is rotated by $\pi/3$ clockwise. (c). $\mu = 0.1$, $K_1 = 0.02$, $K_2 = 10^{-3}$. The interface is rotated by $\pi/6$ counterclockwise. (d). $\mu = 0.05$, $K_1 = 0.1$, $K_2 = 10^{-3}$. The interface is rotated by $\pi/4$ counterclockwise.

h_s is the mesh size of the spline interpolation. Thus to maintain second order accuracy, we need to have roughly $O(h_s^3) \sim O(h^2)$, or $N_b \sim N^{2/3}$. In our simulation, we use roughly $N_b \sim 16 + N^{2/3}$. The number 16 is used to make sure that there are enough initial points on the interface. In Table 1(b), we perform the same experiments but with fewer control points N_b which leads to smaller Schur complement matrix and obviously the condition number becomes slightly smaller. However, the average accuracy orders 2.0221 for the pressure and 3.2110 for the velocity remain about the same.

In Table. 2, we also show how well the interface conditions are satisfied. We can see that all the residuals are relatively small and decrease quadratically for this example. If only five equations are used, the residuals are then proportional to $cond(S)\epsilon$, where ϵ is the machine precision and $cond(S)$ is the condition number of the Schur complement.

4.1.2. Example 2

In the previous example, although the velocity has a tangential slip along the interface but it is a constant in the Darcy's region. Here, we present an example with a continuous tangential velocity but discontinuous pressure along the interface. More importantly, the velocity and pressure are non-trivial in both regions and the normal derivatives of the velocity components are also discontinuous across the interface. The analytic solution of the Navier–Stokes

Table 2
The residual of the six interface conditions (15)–(20) of the computed solution. The last row is the average convergence order of the six interface equations.

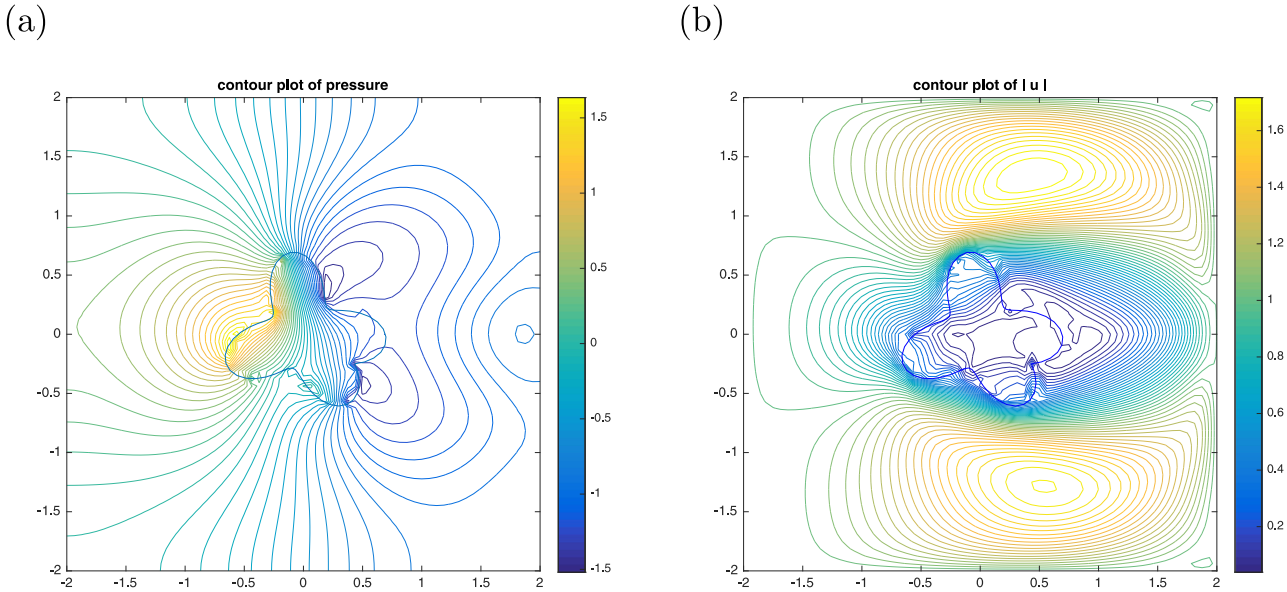| N	$\|E_1\|_\infty^N$	$\|E_2\|_\infty^N$	$\|E_3\|_\infty^N$	$\|E_4\|_\infty^N$	$\|E_5\|_\infty^N$	$\|E_6\|_\infty^N$
32	$3.4972e-03$	$1.8503e-03$	$2.8119e-03$	$4.7202e-03$	$9.7248e-04$	$3.3883e-03$
64	$1.2280e-03$	$5.2899e-04$	$5.1238e-04$	$2.1042e-03$	$2.7033e-04$	$1.0480e-03$
128	$2.0427e-04$	$8.3986e-05$	$8.6997e-05$	$5.9738e-04$	$7.5299e-05$	$1.5937e-04$
256	$2.6319e-05$	$1.2165e-05$	$2.1739e-05$	$9.6036e-05$	$1.5473e-05$	$1.8553e-05$
order	2.5026	2.5091	2.2540	2.0640	2.0642	2.6538

(a)

(b)

Fig. 7. Contour plots of the pressure and the magnitude of the velocity for the geometry with $\mu = 0.05$, $K_1 = 0.1$, $K_2 = 10^{-3}$.

Table 3
A grid refinement analysis of Example 2 at time $T = 0.5$. The parameters are $\mu = 1$, $\rho = 1$, $K_1 = 1$, $K_2 = 2$. The average order of accuracy for the pressure and velocity are 1.8785 and 2.5533, respectively.

N	$\|E_p\|_\infty^N$	order	$\|E_u\|_\infty^N$	order
16	$1.5906e-01$		$4.4836e-02$	
32	$2.8863e-02$	2.4623	$1.1977e-02$	1.9044
64	$9.6539e-03$	1.5800	$2.3634e-03$	2.3413
128	$3.1556e-03$	1.6132	$3.6471e-04$	2.6960
256	$8.7707e-04$	1.8471	$4.8521e-05$	2.9101
512	$2.3669e-04$	1.8897	$6.4358e-06$	2.9144

equations is

$$u_f = g(t)\big(y(x^2 + y^2 - 1) + 2x\big),$$
$$v_f = g(t)\big(-x(x^2 + y^2 - 1) - 2y\big),$$
$$p_f = 3g(t)\big(x^2 - y^2\big), \tag{42}$$

defined outside of the unit circle $x^2 + y^2 = 1$ while the analytic solution for Darcy's system is $u = 2xg(t)$, $v = -2yg(t)$, and $p = -g(t)(x^2 - y^2)$. Again, the source term and the boundary condition are determined from the analytic solution. All the interface conditions are satisfied (after a careful computation) except for the BJS condition which now becomes

$$2\boldsymbol{\tau} \cdot \mathbf{D}_f \cdot \mathbf{n} = 2\big(\mathbf{u}_f - \mathbf{u}_D\big) \cdot \boldsymbol{\tau} + 2g(t)(8xy + 2). \tag{43}$$

That is, we have $K_2 = 2$ and a non-homogeneous BJS condition. Our method is flexible in dealing with different interface conditions by simply modifying the interpolation scheme. In Table 3, we show a grid refinement analysis for the above example with $g(t) = e^{-t}$.

The solution is computed up to $T = 0.5$. The average order of accuracy for the pressure and velocity are 1.8785 and 2.5533, respectively.

4.1.3. Comparison results for the Stokes and Darcy coupling

In this subsection, we show some comparison results obtained from the present method and the one in [27] for solving the Stokes and Darcy coupling equations. We use the same analytic solutions as presented in previous Example 1 and 2 with $g(t) \equiv 1$ so that the problems become stationary ones that satisfy the Stokes and Darcy coupling equations. We can conclude that the new method outperforms the previous one in all aspects including accuracy.

In Table 4, we compare the maximum norm errors in the computed pressure and velocity and their average accuracy orders through a grid refinement analysis for Example 1 with $g(t) \equiv 1$. Although the errors (in the pressure and velocity) obtained by the present method are slightly smaller than the ones obtained by the previous method; however the average order of accuracy for the pressure obtained by the present method is almost second order compared to the first order obtained using the method in [27]. Furthermore, as before, the condition number of the Schur complement matrix for the present method is significantly smaller than the one in [27] as shown in Table 4(c).

It is well-known that using Cartesian grid methods to solve the interface problems, the computed errors do not necessarily decrease monotonically because the relative location of the underlying grid and the interface keeps changing with different meshes. More precisely speaking, if the error happens to be $O(h^2) \sim Ch^2$, then the error constant C, while it is $O(1)$, will depend on the mesh size h. That is why the order often fluctuates and we use the average order of accuracy instead.

Table 4

A comparison of numerical results obtained by the present method and the one in [27] for Example 1 with $g(t) = 1$. (a) The average of the accuracy order for the pressure is 1.7839 (present) and 1.2145 [27], respectively. (b) The average of the accuracy order for the velocity is 1.9688 (present) and 2.0241 [27], respectively. (c) A list of the condition number of the Schur complement matrix.

(a) Comparison of the pressure error and accuracy order.

$N = N_b$	$\|E_p^{6eq}\|_\infty^N$ (present)	order	$\|E_p^{5eq}\|_\infty^N$ [27]	order
32	$9.1289e-03$		$2.7892e-02$	
64	$1.9969e-03$	2.1927	$6.0515e-03$	0.37889
128	$9.9901e-04$	0.9918	$3.2848e-03$	0.88149
256	$3.6806e-04$	1.4406	$3.2848e-03$	0.88149
512	$6.4588e-05$	2.5106	$9.6182e-04$	1.7720

(b) Comparison of velocity error and accuracy order.

N	$\|E_\mathbf{u}^{6eq}\|_\infty^N$ (present)	order	$\|E_\mathbf{u}^{5eq}\|_\infty^N$ [27]	order
32	$2.1160e-02$		$3.2203e-02$	
64	$5.8094e-03$	1.8649	$1.4188e-02$	1.1825
128	$1.4762e-03$	1.9765	$2.6563e-03$	2.4172
256	$3.3356e-04$	2.1459	$1.2963e-03$	1.0350
512	$9.0142e-05$	1.8877	$2.5613e-04$	2.3395

(c) Comparison of the condition number.

$N = N_b$	$cond^{6eq}$ (present)	$cond^{5eq}$ [27]
32	$5.1733e+02$	$1.6935e+06$
64	$3.1495e+03$	$1.8021e+06$
128	$3.3617e+04$	$1.2956e+08$
256	$2.5181e+05$	$2.2210e+09$
512	$2.3641e+06$	$1.5831e+11$

Table 5

A comparison of numerical results obtained by the present method and the previous one in [27] for Example 2 with $g(t) = 1$. (a) The average of accuracy order for the pressure is 1.9546 (present) and 1.0290 ([27]), respectively. (b) The average of accuracy order for the velocity is 2.0089 (present) and 1.3991 ([27]), respectively. (c) A list the condition number for the Schur complement matrix.

(a) Comparison of pressure error and accuracy order.

$N = N_b$	$\|E_p^{6eq}\|_\infty$ (present)	order	$\|E_p^{5eq}\|_\infty$ [27]	order
32	$1.9872e-02$		$4.5180e-02$	
64	$4.6398e-03$	2.0986	$1.9400e-02$	1.2196
128	$1.1274e-03$	2.0411	$7.4437e-03$	1.3820
256	$3.9083e-04$	1.5284	$3.7226e-03$	0.9997
512	$8.8040e-05$	2.1503	$O(1)$	–

(b) Comparison of velocity error and accuracy order.

N	$\|E_u^{6eq}\|_\infty$ (present)	order	$\|E_u^{5eq}\|_\infty$ [27]	order
32	$4.0806e-03$		$2.1728e-02$	
64	$4.7210e-04$	1.4227	$7.7453e-03$	1.4881
128	$5.9990e-05$	2.1886	$2.5090e-03$	1.6262
256	$6.2950e-06$	2.1895	$1.3202e-03$	0.9263
512	$1.7430e-06$	2.2348	$O(1)$	–

(c) Comparison of the condition number.

$N = N_b$	$cond^{6eq}$ (present)	$cond^{5eq}$ [27]
32	$1.4182e+02$	$1.9853e+03$
64	$6.0734e+02$	$1.9853e+03$
128	$2.5750e+04$	$3.6590e+05$
256	$2.6958e+05$	$7.6613e+06$
512	$2.0434e+06$	$1.2118e+08$

Table 5 shows the comparison between those two methods for Example 2 with $g(t) = 1$. As we can observe that from Table 5(b), the error difference in the velocity is more profound. The average accuracy orders for the pressure obtained from the present method and the one in [27] are 1.9546 and 1.0290; while for the velocity are 2.0089 and 1.3991, respectively. Furthermore, the method in [27] failed to yield meaningful results with the fine grid ($N = 512$) since both the pressure and velocity have $O(1)$ errors

due to the bad conditioning of the linear system that eventually destroys the convergence. This comparison once again shows the out-performance of the present method over the one in [27].

For stationary Stokes and Darcy coupling equations, both the five-equation and six-equation approaches work well for computed velocity as long as double precision is used. The trade-off of the six-equation approach is more computational complexity in solving the discrete problem. We need to solve a rectangular linear system of equations for the augmented variables. Nevertheless, the additional computational cost is well worthy because (1) the equivalence of the original and transformed problem is almost automatically established; (2) the extra augmented equation makes the linear system more well-conditioned; (3) the computed pressure is also second order accurate in the L^∞ norm in addition to second order accurate velocity, see for example, Table 1–5; (4) without this extra constraint, the method in [27] barely works for the Navier–Stokes and Darcy coupling. Numerically, we use the projection step to enforce the divergence condition in the interior of the flow and enforce the divergence condition at the boundary and interface as an additional augmented equation.

5. Flow simulations

Now we perform some flow simulations of the Navier–Stokes and Darcy coupling in which a given flow entering the domain from the left side of the rectangular domain ($[-2, 2] \times [-2, 2]$). Some similar simulations have been done for the Stokes and Darcy coupling in [27]. In Fig. 2, we show results for different parameters and interfaces in which the porous media is inside the interface. The inflow condition is $u = 1$, $v = 0$. For small Reynolds numbers and velocities, the results are similar to the Stokes and Dacry coupling. In Fig. 2(a), the interface is $x^2/0.6^2 + y^2/0.4^2 = 1$, $\mu = 1$, $K_1 = 0.02$, $K_2 = 1$, and the final time is $T = 6.5$. The flow is nearly tangent to the interface. In Fig. 2(b), the setup is the same except that the ellipse is rotated. In general, the larger K_1, the easier that the fluid can go through the interface. In Fig. 2(c), we deliberately choose very small $K_2 = 10^{-6}$ so that the velocity is almost continuous in the tangential direction of the interface $r = 0.5 + 0.1 \sin 5\theta$ in the polar coordinates. The interface is nearly invisible to the fluid. The other parameters are $\mu = 1$, $K_1 = 0.02$, and the final time $T = 6.5$. In Fig. 2(d), we show the result for the same interface with $\mu = 1$, $K_1 = 0.02$, $K_2 = 1.3$, and the final time is $T = 6.5$. In Fig. 3, we show some simulation results for a porous media flow outside while a fluid flow inside the interface with different fixed interfaces. We compare the result of the Darcy and Stokes coupling in Fig. 3(a) with that of the Darcy and Navier–Stokes coupling in Fig. 3(b) at the final time $T = 0.5$. The parameters are $\mu = 0.2$, $K_1 = 0.05$, $K_2 = 1.3$, and the interface is $r = 0.5 + 0.1 \sin 5\theta$ in the polar coordinates. We observe that the flow patterns are slightly different near the left and right intrusions of the interface while they are similar in other parts of the domain. Fig. 3(c) shows a simulation with $\mu = 0.02$, $K_1 = 0.5$, and $K_2 = 1.3$. The interface is $x^2/0.4^2 + y^2/0.6^2 = 1$. Fig. 3(d) shows a simulation with a five star-shape interface $r = 0.5 + 0.2 \sin 5\theta$ that has deeper petals. The parameters are $\mu = 0.02$, $K_1 = 0.5$, and $K_2 = 1.3$, and the final time $T = 0.5$.

Once again, in Table 6 we show how well the interface conditions are satisfied for the simulation of Fig. 3(b). We can see that all the residuals are relatively small and decrease between linearly and quadratically.

Next, we carry out numerical experiments of a coupling flow with an interface that has corners as shown in Fig. 4 with different parameters at the final time $T = 3.5$. The interface is represented by a closed cubic spline interpolation and thus the corners are smoothed out to some extent but we have enough points near the corners to keep it sharp. In Fig. 4(a) and (b), the Navier–Stokes

Table 6
A grid refinement analysis for the residual of interface relations for the simulation of Fig. 3(b). The last row is the average convergence order for the six interface equations.

N	$\|E_1\|_\infty^N$	$\|E_2\|_\infty^N$	$\|E_3\|_\infty^N$	$\|E_4\|_\infty^N$	$\|E_5\|_\infty^N$	$\|E_6\|_\infty^N$
32	$6.3003e-02$	$4.6426e-02$	$2.0108e-01$	$1.4004e-02$	$1.0080e-01$	$4.8634e-02$
64	$2.0564e-02$	$1.2779e-02$	$4.5375e-02$	$2.4405e-03$	$1.8869e-02$	$1.5302e-02$
128	$5.6672e-03$	$2.5794e-03$	$2.6441e-02$	$1.4941e-03$	$7.0059e-03$	$3.5652e-03$
256	$1.7352e-03$	$8.7961e-04$	$9.4399e-03$	$6.9989e-04$	$1.9501e-03$	$9.5656e-04$
order	1.7274	1.9073	1.4710	1.4409	1.8973	1.8893

flow is outside the triangle while the Darcy's law is inside. We can see that some corners act as a sink with large velocity there. In Fig. 4(a), the parameters are $\mu = 0.1$, $K_1 = 0.02$, and $K_2 = 10^{-4}$. The largest velocity appears at the top corner. In Fig. 4(b), the triangle has been rotated by $\pi/4$ counterclockwise. The parameters are $\mu = 0.1$, $K_1 = 0.02$, and $K_2 = 10^{-3}$. The largest velocity appears now at the bottom corner. In Fig. 4(c)-(d), we have the Darcy's law outside the triangle while the Navier–Stokes flow is inside. In Fig. 4(c), the parameters are $\mu = 0.02$, $K_1 = 0.25$, and $K_2 = 1.3$. The bottom corner acts like a sink. In Fig. 4(d), the parameters are $\mu = 0.02$, $K_1 = 0.5$, and $K_2 = 10^{-4}$, which makes the velocity a smaller jump in the tangent direction. While the flow gets more penetrated in, the behavior is similar to the case in Fig. 4(c).

5.1. Effect of the shape and orientation of the interface on the flow

Next, we show some simulation results on the effect of the shape and orientation of the interface. We start with the case that the Darcy's law is outside and a fluid flow is inside. We show an interface that has large curvature at some parts which looks like corners. Some part of the interface is convex while other part is concave. We also rotate the interface in different directions to investigate how the orientation of the interface affects the flow. As we observe already that the larger K_1 is, the easier the flow can penetrate through the interface; the smaller K_2 is, the closer of the velocity in two regions across the interface since there is less jump in the velocity in the tangential direction. In Fig. 5, we have an interface with symmetry in the x-axis. In Fig. 5(a), the parameters are $\mu = 0.1$, $K_1 = 0.5$, $K_2 = 10^{-4}$. The flow penetrate the part of interface that is closer to the left boundary. The velocity is larger in the fluid region at the part of the interface that is closer to the left and right boundary. The velocity remains symmetric with respect to the x-axis. In Fig. 5(b), the interface is same as in Fig. 5(a) but is rotated by $\pi/6$ counterclockwise. The parameters are $\mu = 0.002$, $K_1 = 0.02$, $K_2 = 10^{-3}$. Once again, we observe that the velocity is larger in the fluid region near the part of the interface that is closer to the left and right boundary but not to the top or bottom boundary. In Fig. 5(c), the parameters are $\mu = 0.002$, $K_1 = 0.02$, $K_2 = 10^{-3}$. The interface is rotated by $\pi/3$ counterclockwise. In Fig. 5(d), the parameters are $\mu = 0.002$, $K_1 = 0.02$, $K_2 = 10^{-3}$. The interface is rotated by $3\pi/4$ clockwise. In the last two plots, we observe that the main stream of the flow is along the elongated directions of the fluid region. The the corner-liked geometry has little effect on the flow since it is in a concave part of the interface.

In Fig. 6, we have an interface that has the same shape as in Fig. 5(a) except that the interface is scaled down to have more flow region outside, which has more influences on the flow. In Fig. 6(a), the parameters are $\mu = 0.1$, $K_1 = 0.02$, $K_2 = 10^{-3}$. The magnitude of the velocity is large in the fluid region near the protrusion part of the interface. The flow remains symmetric with respect to the x-axis. In Fig. 6(b), the interface is same as in Fig. 6(a) but is rotated by $\pi/3$ clockwise. The parameters are $\mu = 0.1$, $K_1 = 0.02$, $K_2 = 10^{-3}$. In Fig. 6(c), the parameters are $\mu = 0.1$, $K_1 = 0.02$, $K_2 = 10^{-3}$. The interface is rotated by $\pi/3$ counter clockwise. In Fig. 6(d),

Table 7
A grid refinement analysis for Fig. 6(b) against the solution at a fine grid $N = 512$. The average order of accuracy for the pressure and velocity are 1.5172 and 1.6115, respectively. We do see the convergence order of the velocity increases as the mesh gets finer.

N	$\|E_p\|_\infty^N$	order	$\|E_u\|_\infty^N$	order
32	3.4617		$5.5640e-01$	
64	2.3213	0.5765	$2.4552e-01$	1.1803
128	1.2955	0.8414	$7.8180e-02$	1.6510
256	$1.4760e-01$	3.1337	$1.9502e-02$	2.0032

the parameters are $\mu = 0.005$, $K_1 = 0.1$, $K_2 = 10^{-3}$. The interface is rotated by $\pi/4$ counter clockwise. In Fig. 6(c) and (d), we observe that the protrusion of the interface facing the upstream affects the flow pattern more significantly than that of the protrusion facing the downstream. The symmetry is also lost due to the rotations. Once again the corner-liked geometry has little effect on the flow since it is a concave part of the interface.

For the flow problem, analytic solutions are not available. In Table 7, we show a grid refinement analysis against the solution obtained from a fine grid $N = 512 \times 512$ with $N_b = 256$. We observe a super-linear convergence for both the pressure and velocity. We think the second order convergence is affected by the large curvature at some part of the interface. As the mesh gets finer, the convergence also improves.

In Table 8, we show how well the interface conditions are satisfied for the simulation of Fig. 6(b). We can see that all the residuals are relatively small and decrease in a super-linear fashion. Compared with the results earlier, the larger curvature may affect the convergence.

For a similar geometry and set-up, we show the contour plots of the pressure and the magnitude of the velocity in Fig. 7. We observe that the pressure and magnitude of the velocity have large gradient (denser contour lines) near the interface, particularly at the places where the interface has large curvatures.

5.2. Simulations with time transient behaviors

Finally, we show an example with a time dependent boundary condition, which cannot be solved by the method proposed in [27] for the stationary Stokes and Darcy coupling. We assume that we have a time-dependent source/sink inflow from the left. The boundary condition at the left boundary $(x = -2)$ is $u(-2, y, t) = \cos(\pi y/4 + \pi t/2)$ and $v = 0$. At the top and bottom boundaries, we set $u(-2, \pm 2, t) = \cos(\pm \pi/2 + \pi t/2)$ and $v = 0$. At the right boundary, we use a simple Neumann boundary condition $\frac{\partial u}{\partial x} = 0$ and $\frac{\partial v}{\partial x} = 0$. The parameters are $\mu = 0.1$, $K_1 = 0.02$, $K_2 = 10^{-3}$. The mesh size is $N = 128$ and $N_b = 90$.

In Fig. 8, we show several snapshots of the velocity at different times, $t = 3$, $t = 3.5$, $t = 4$, $t = 4.5$, $t = 5$, $t = 5.5$, $t = 5.75$, and $t = 6$. We also check how well the interface relations are satisfied. Due to the corner singularity where the normal derivative is not well defined, we obtain only $O(1)$ convergence for the residual of the interface relations which is predictable. in Fig. 9, we show the
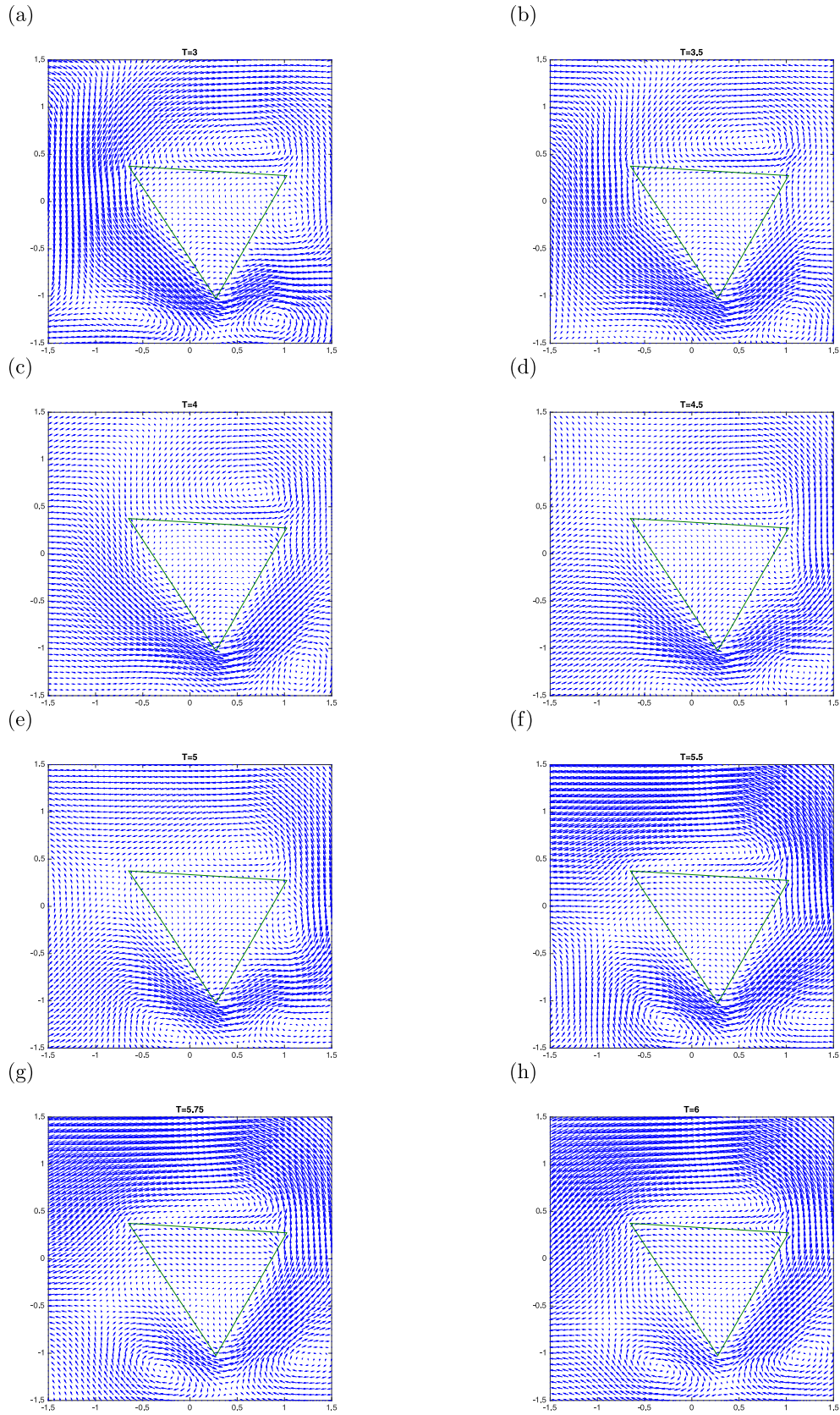
(a)

(b)

(c)

(d)

(e)

(f)

(g)

(h)

Fig. 8. The snapshots of the Navier–Stokes and Darcy coupling with a triangle interface. The Navier–Stokes flow is defined outside of the interface while the Darcy's law is defined inside. The time-dependent inflow condition is applied from the left boundary. $\mu = 0.1$, $K_1 = 0.02$, $K_2 = 10^{-3}$.

Table 8
A grid refinement analysis for the residual of interface relations for the simulation of Fig. 6(b). The last row is the average convergence order for the six equations.

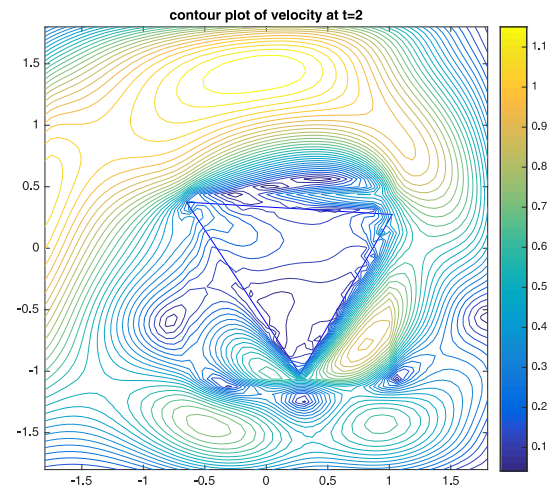| N	$\|E_1\|_\infty^N$	$\|E_2\|_\infty^N$	$\|E_3\|_\infty^N$	$\|E_4\|_\infty^N$	$\|E_5\|_\infty^N$	$\|E_6\|_\infty^N$
32	$6.0957e-02$	$2.5018e-02$	$1.8512e-01$	$1.0282e-02$	$1.0788e-01$	$6.6820e-02$
64	$1.9720e-02$	$7.4305e-03$	$3.5630e-02$	$1.2220e-03$	$1.3194e-02$	$1.4806e-02$
128	$5.1510e-03$	$2.8693e-03$	$2.1406e-02$	$2.1599e-03$	$9.3172e-03$	$4.0977e-03$
256	$2.6799e-03$	$1.8443e-03$	$1.5249e-02$	$9.6179e-04$	$2.1174e-03$	$2.0506e-03$
order	1.5025	1.2539	1.2006	1.1394	1.8903	1.6754
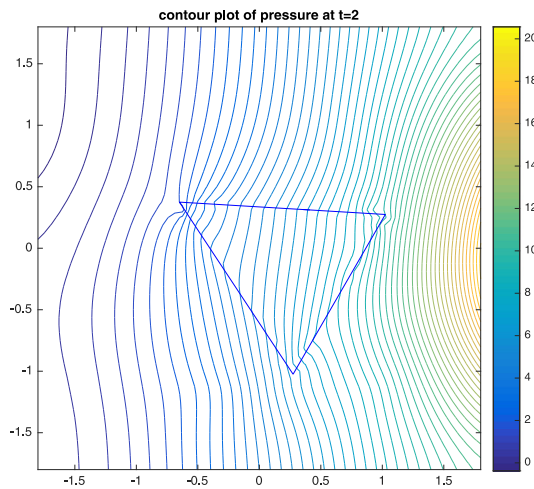
(a) (b)

Fig. 9. Contour plots of the pressure and the magnitude of the velocity at $t = 2$ with the set-up in Fig. 8.

contour plots of the pressure and the magnitude of the velocity. The pressure tends to composed of two smooth functions since the pressure is the solution of a Poisson equation in each sub-domain, while the velocity tends to have more variations due to the corner singularity and the non-linear effect which cause the flow separation along the edges and vortex shading away from the edges. The simulations may have potential values for controlling of fluid flows through porous media materials.

6. Conclusions

In this paper, we propose a new Cartesian finite difference method for solving a coupled system of a fluid flow modelled by the Navier–Stokes equations and a porous media modelled by the Darcy law, respectively. Numerical results show that both the computed pressure and velocity are second order accurate in the maximum norm for the problems with known analytic solutions. The new method can also guarantee the equivalence of the solutions between the original and the transformed problem under certain regularity assumptions though the sensitivity analysis of the new system is still an open question. The new approach has also been applied to the Stokes and Darcy coupling, which outperforms the method proposed in [27] in almost all the categories. For Navier–Stokes and Darcy coupling equations, we observe that the shape of the interface may have significant effects on the coupling especially in the fluid region. The fluid flow is likely to be elongated along the direction of the objects of the porous media and has more variations at corners due to the corner singularity and the non-linear effect which can cause flow separations along edges and vortex shedding away from edges.

References

[1] D'Angelo C, Zunino P. Robust numerical approximation of coupled Stokes' and Darcy's flows applied to vascular hemodynamics and biochemical transport. ESAIM Math Model Numer Anal 2011;45:447–76.
[2] Arbogast T, Brunson DD. A computational method for approximating a Darcy–Stokes system governing a vuggy porous medium. Comput Geosci 2007;11(3):207–18.
[3] Arbogast T, Gomez M. A discretization and multigrid solver for a Darcy–Stokes system of three dimensional vuggy porous media. Comput Geosci 2009;13(3):331–48.
[4] Babuška I, Gatica GN. A residual-based a posteriori error estimator for the Stokes–Darcy coupled problem. SIAM J Numer Anal 2010;48(2):498–523.
[5] Badea L, Discacciati M, Quarteroni A. Numerical analysis of the Navier–Stokes—Darcy coupling.. Numer Math 2010;115(2):195–227.
[6] Beale JT, Layton AT. On the accuracy of finite difference methods for elliptic problems with interfaces. Commun Appl Math Comput Sci 2006;1:91–119.
[7] Boubendir Y, Tlupova S. Stokes–Darcy boundary integral solutions using preconditioners.. J Comput Phys 2009;228(23):8627–41.
[8] Cai M, Mu M, Xu J. Numerical solution to a mixed Navier–Stokes–Darcy model by the two-grid approach. SIAM J Numer Anal 2009;47(5):3325–38.
[9] Cai M, Mu M, Xu J. Preconditioning techniques for a mixed Stokes–Darcy model in porous media applications. J Comput Phys 2009;233(2):346–55.
[10] Cao Y, Gunzburger M, He X, Hua F, Wang X, Zhao W. Finite element approximation for Stokes–Darcy flow with Beavers–Joseph interface conditions. SIAM J Numer Anal 2010;47(6):4239–56.

[11] Çeşmelioğlu A, Rivière B. Analysis of time-dependent Navier–Stokes flow coupled with Darcy flow. J Numer Math 2008;16(4):249–80. MR2493168 (2009m:35375).

[12] Chen W, Chen P, Gunzburger M, Yan N. Superconvergence analysis of femsfor the Stokes–Darcy system. Math Methods Appl 2010;33(13):1605–17.

[13] Chidyagwai P, Rivière B. On the solution of the coupled Navier–Stokes and Darcy equations. Comput Methods Appl Mech Eng 2009;198(47–48):3806–20. 2557499 (2010j:76038).

[14] DAngelo C, Zunino P. Numerical approximation with Nitsche's coupling of transient Stokes'/Darcy's flow problems applied to hemodynamics. Appl Numer Math 2012;62(4):378–95.

[15] Discacciati M, Miglio E, Quarteroni A. Mathematical and numerical models for coupling surface and groundwater flows. Appl Numer Math 2002;43(1–2):57–74. 19th Dundee Biennial Conference on Numerical Analysis (2001). MR1936102 (2003h:76087).

[16] Discacciati M, Quarteroni A. Convergence analysis of a subdomain iterative method for the finite element approximation of the coupling of stokes and Darcy equations. Comput Vis Sci 2004;6(2–3):93–103. MR2061270 (2005e:65142).

[17] Ervin VJ. Approximation of coupled Stokes–Darcy flow in an axisymmetric domain. Comput Methods Appl Mech Eng 2013;258:96–108. MR3047902.

[18] Ferreira JA, Barbeiro S, Pena G, Wheeler MF. Modelling and simulation in fluid dynamics in porous media. In: Springer Proceedings in Mathematics Statistics, 28. Springer, New York; 2013. Selected papers from the Workshop on Fluid Dynamics in Porous Media held in Coimbra, September 12–14, 2011. MR3075010.

[19] Gatica GN, Meddahi S, Oyarzúa R. A conforming mixed finite-element method for the coupling of fluid flow with porous media flow. IMA J Numer Anal 2009;29(1):86–108.

[20] Girault V, Kanschat G, Rivière B. On the coupling of incompressible stokes or Navier–Stokes and Darcy flow through porous media. In: Modelling and simulation in fluid dynamics in porous media. Springer Proc. Math. Stat., vol. 28. Springer, New York; 2013. p. 1–25. MR3065684.

[21] Johnston H, Liu J. Finite difference schemes for incompressible flow based on local pressure boundary conditions. J Comput Phys 2002;180:120–54.

[22] Johnston H, Liu J. Accurate, stable and efficient Navier–Stokes solvers based on explicit treatment of the pressure term. J Comput Phys 2004;188:221–59.

[23] Kanschat G, Rivière B. A strongly conservative finite element method for the coupling of Stokes and Darcy flow. J Comput Phys 2010;229(17):5933–43. MR2657851 (2011h:76081).

[24] Karper T, Mardal KA, Winther R. Unified finite element discretizations of coupled Darcy–Stokes flow. Methods Partial Differ Equ 2009;25(2):311–26.

[25] Layton WJ, Schieweck F, Yotov I. Coupling fluid flow with porous media flow. SIAM J Numer Anal 2002;40(6):2195–218.

[26] LeVeque RJ, Li Z. The immersed interface method for elliptic equations with discontinuous coefficients and singular sources. SIAM J Numer Anal 1994;31:1019–44.

[27] Li Z. An augmented Cartesian grid method for Stokes–Darcy fluid structure interactions. Int J Numer Methods Eng 2015;106(7):556–75.

[28] Li Z. IIMPACK: a collection of fortran codes for interface problems. Anonymous ftp at ftp.ncsu.edu under the directory: /pub/math/zhilin/Package and http://www4.ncsu.edu/~zhilin/IIM, last updated: 2016.

[29] Li Z, Ito K. The immersed interface method – numerical solutions of PDEs involving interfaces and irregular domains. SIAM Frontier Series in Applied mathematics, FR33; 2006.

[30] Li Z, Wan X, Ito K, Lubkin S. An augmented pressure boundary condition for a stokes flow with a non-slip boundary condition. Commun Comput Phys 2006;1:874–85.

[31] Li Z, Xi L, Cai Q, Zhao H, Luo R. A semi-implicit augmented IIM for Navier–Stokes equations with open and traction boundary conditions. J Comput Phys 2015;297:182–93.

[32] Mu M, Xu J. A two-grid method of a mixed Stokes–Darcy model for coupling fluid flow with porous media flow. SIAM J Numer Anal 2007;45(5):1801–13. MR2346360 (2008i:65264).

[33] Pacquaut G, Bruchon J, Moulin N, Drapier S. Combining a level-set method and a mixed stabilized p1/p1 formulation for coupling Stokes–Darcy flows. Int J Numer Methods Fluids 2012;69(2):459–80. MR2912610.

[34] Tlupova S, Cortez R. Boundary integral solutions of coupled Stokes and Darcy flows. J Comput Phys 2009;228(1):158–79. MR2464074 (2009j:76168).

[35] Vassilev D, Yotov I. Coupling Stokes–Darcy flow with transport. SIAM J Sci Comput 2009;31(5):3661–84. MR2556557 (2011c:76105).

[36] Wang Z, Lubkin SR, Li Z. A robin-robin domain decomposition method for a Stokes–Darcy structure interaction with locally modified mesh. Numer Math Theory Meth Appl 2014;7(4):435–46.